

Dynamical scaling laws revealed by parametric temporal cutoffs

Ceren B. Dağ* and Kai Sun

Department of Physics, University of Michigan, Ann Arbor, Michigan 48109, USA

(Dated: June 18, 2022)

Dynamical phase transitions (DPTs) are generally defined under two different but known-to-be related categories: DPT-I where the equilibrium value (or long-time average) of the order parameter as a function of the control parameter demonstrates a phase boundary; DPT-II where the Loschmidt return rate shows a cusp singularity in real-time dynamics. In this Letter, we introduce a quantum phase transition *far from equilibrium* based on a parametric temporal cutoff whose form can be derived from the velocity bounds of the system. We find that far away from the equilibrium, two-time correlators at the cutoff could exhibit order parameterlike behavior in analogy to equilibrium quantum criticality, i.e. zero in the disordered phase and nonzero with a power-law scaling once the control parameter reaches a critical boundary. For the integrable Ising model, the dynamic phase boundary coincides with the transition point of the underlying equilibrium transition, although the system is initially prepared in a fully polarized state. Once the integrability is broken, dynamical order persists with phase boundary shifted from the equilibrium one. The scaling dimension of the observed power-law scaling differs from the Ising universality class and its value changes as one moves away from integrability. Our results point to true nonequilibrium criticality and we elucidate the origin of this novel dynamic transition by studying the hierarchy of timescales in the dynamical response.

Introduction. Criticality, defined under Landau paradigm [1], is one of the milestones in our understanding of matter, providing us a framework to classify microscopically diverse phenomena in a handful of universality classes with their associated critical exponents [2, 3]. Its dynamical counterpart, dynamical criticality, studies both the imprints of equilibrium criticality on dynamics [4–14] and genuine non-equilibrium criticality that does not necessarily originate from an equilibrium transition [11, 12, 15–21]. Dynamical phase transitions (DPT) could in general be classified via two different but related definitions [11, 19]: DPT-I and DPT-II. DPT-I is defined based on the time evolution of an (equilibrium) order parameter quenched from a state that is not an eigenstate of the evolution Hamiltonian [11]. In the ordered phase where the control parameter originates from the equilibrium transition, a prethermal regime appears with either equilibration or oscillatory saturation. Hence the long-time average of the signal could act like a dynamical order parameter, demonstrating a phase boundary. DPT-II concerns with cusp singularity appearing at critical times of the return rate that is based on Loschmidt echo and is linked to equilibrium phase transitions [9–11]. Here, we introduce a new family of dynamical quantum phase transition (QPT) *far from equilibrium*. In particular, we focus on systems that do not exhibit conventional DPTs, i.e. systems with short range couplings [12, 19], where the saturation value of their two-time correlators (TTC) are known to be featureless [22–24]. Dynamical order seems to persist steadily only for long range interacting models [18, 19]; or when we utilize infinite-time averages of OTOCs [12] or equal-time correlators additionally averaged over space [21] in short range systems. However TTCs are simpler objects than both OTOCs and equal-

time correlators averaged over space, and hence their experimental realizations, in particular with polarized initial states, are much convenient to realize in quantum simulators of various media, e.g. cold atoms, ion traps, superconducting qubits [20, 25–29].

All these observations about TTCs motivate us in this study to show that TTCs in local systems are actually not oblivious to dynamical phase transitions; instead they require a new DPT definition that *respects their hierarchy of timescales*. We find that instead of the conventional cutoff on time, $t \sim N$ where the interval of time is proportional to the system size and corresponds to effectively infinite-time limit for finite sizes; we could study late times, t_L defined with a parametric temporal cutoff based on the maximum propagation velocity of excitations. Defining a DPT based on late times, which is clearly shorter than $t \sim N$, eventually presents us a well-defined dynamic phase boundary for local Hamiltonians measured with TTCs; meaning that (i) we mark a transition point, (ii) we find a power-law scaling with an associated scaling exponent for the dynamic order parameter of TTC. Given in an equilibrium QPT, finite-size effects become significant as the system critically slows down with a diverging correlation length, and hence finite-size scaling is applied to mark down the phase boundary in finite-size numerical simulations [30]. However the new DPT exhibits data collapse leading to a power-law scaling with no need for finite-size scaling, because the finite-size effects and system size dependence vanish as soon as moderate system size is reached. Later we reveal that the parametric temporal cutoff coincides with collapse timescale of dynamic response and the dynamic order parameter is contributed by many excited states, not only in the low energy sector of the energy spectrum; all of which demonstrates the true nonequilibrium origin of our

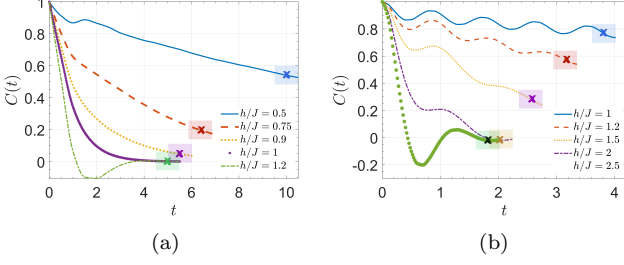


FIG. 1. $C(t)$ plotted until its late timescale only for different h via t-DMRG (density matrix renormalization group) (a) at $N = 36$ for $\Delta = 0$ TFIM and (b) at $N = 30$ for $\Delta = -1$ TFIM. The crosses mark the late timescales defined in the text and the translucent blocks around them are the data intervals, $t_L \pm 0.5$, where we collect data and study the DPT.

definition.

Definition. A TTC is $C(t) = \langle \psi_0 | \sigma_r^z(t) \sigma_r^z | \psi_0 \rangle$ where $|\psi_0\rangle = |\uparrow\uparrow \dots \uparrow\rangle$ is a polarized state and σ_r^z is a local spin operator of a bulk spin. Let us introduce TFIM with both nearest-neighbor (NN) and next-nearest-neighbor (NNN) couplings,

$$H = -J \sum_r \sigma_r^z \sigma_{r+1}^z - \Delta \sum_r \sigma_r^z \sigma_{r+2}^z + h \sum_r \sigma_r^x, \quad (1)$$

with open boundaries and where σ_r^α are spin- $\frac{1}{2}$ Pauli spin matrices. TFIM preserves its gapped long-range Ising ground state even when the interactions (or non-integrability) Δ are introduced, although the transition boundary shifts to favor order as Δ increases.

Given the most basic difference between thermalization (via TTC) and scrambling (via OTOCs) is their time-scales, we question whether the timescale of TTC in exhibiting dynamical order could be different than OTOCs', i.e. could we define a *temporal cutoff* that could capture a dynamical order before finite-size effects appear in TTC? The observation that the order in TTC vanishes as the system size increases, [12, 19, 31] suggests that the conventional temporal cutoff $t \sim N$ does not respect the hierarchy of timescales specific to TTC, and hence the finite-size effects do appear in dynamic phase diagram. We note that the hierarchy of timescales of two-point correlators are discussed in Ref. [23] for asymptotically far away spins in (integrable, $\Delta = 0$) TFIM, $l \rightarrow \infty$ based on the quasi-particle velocity v_q . As will be utilized later, equal-time two-point correlators show light-cone effect [32–35], however TTCs do not. Hence in the following definition for a hierarchy of timescales in TTC, we set the space dimension to unity $l = 1$. Then we obtain, (i) short times, $t \ll 1/v_{max}$; (ii) intermediate times $t \sim 1/v_{max}$ and (iii) late times $t \gg 1/v_{max}$, where v_{max} is the maximum quasi-particle velocity, $v_{max} = \max|\epsilon(h, k)/dk| = 2J\min(h, 1)$ because the dispersion of TFIM reads $\epsilon(h, k) = 2J\sqrt{1 + h^2 - 2h\cos(k)}$ [3]. Hence

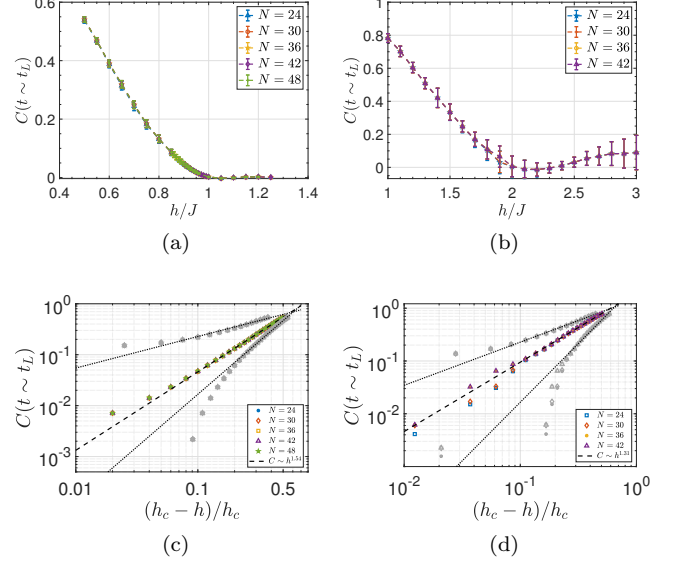


FIG. 2. The DPT applied to TFIM (a) $\Delta = 0$ and (b) $\Delta = -1$ shown with different system sizes $N = 24, 30, \dots, 48$ all collapsing on each other, suggesting a power-law scaling with h in the ordered phase. The best power-law scaling mark the dynamic phase boundary for (c) $\Delta = 0$ as $h/J = 1$ with scaling exponent of $\beta_d = 1.54$ and (d) $\Delta = -1$ as $h/J = 2.025$ with scaling exponent of $\beta_d = 1.31$.

late timescale of TTC reads, more explicitly,

$$t_L(h) \gg \frac{1}{2J\min(h, 1)} \rightarrow t_L(h) \gtrsim \frac{5}{\min(h, 1)}, \quad J = 1. \quad (2)$$

Red-solid curve in Fig. 3a shows the functional form of this *h-parametrized temporal cutoff*, providing us a late timescale for TTC in integrable TFIM which is based on the most energetic excitation that the system can host. We note that a TTC in its late time-scale does not necessarily exhibit an explicit saturation regime, instead could seem to be in a transient response, as it is generally the case for the ordered phase. In Fig. 1a, we plot dynamic responses of various h parameters and mark with colorful crosses where the late timescale kicks in. As it would be more experimentally convenient, we do not only collect point data, but instead an interval of data as $t_L(h) \pm 0.5$ and show the data interval with translucent-colored boxes. While not time-averaging the dynamic response and instead collecting a small interval of data around the late timescale do not only make our scheme distinct from DPT-I scheme, but also render the dynamical order emerging out of this procedure genuinely non-equilibrium. We demonstrate in the Supplement [31] how our data is indeed different than ground state (GS) contribution in the emergent dynamical order, where GS contribution vanishes as system size increases [12, 19, 31]. On the other hand, our procedure results in a well-defined dynamic phase boundary, Fig. 2a, where the data of various system sizes collapse on each other. Further, we ob-

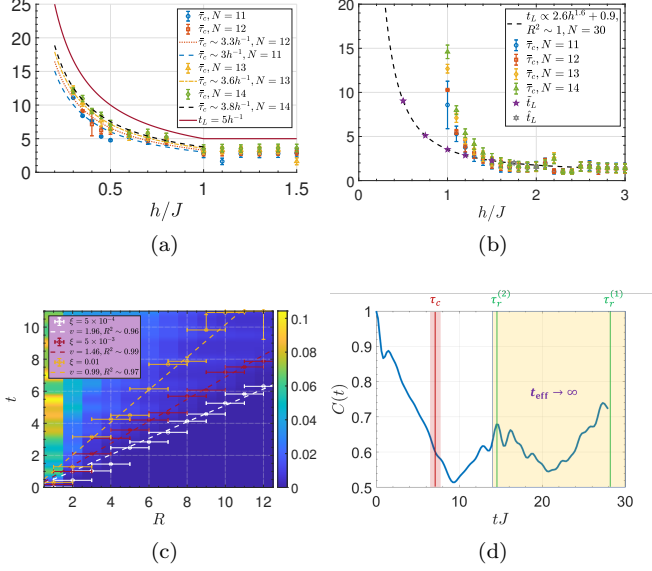


FIG. 3. (a) $\Delta = 0$ TFIM: Late time t_L based on analytic h -parametrized cutoff on time with red-solid line ($N \rightarrow \infty$); compared to estimated collapse time-scales for different system sizes ranging between $N = 11$ –14. (b) $\Delta = -1$ TFIM: t_L fit is shown with black-dashed line and data with both purple-pentagrams and grey-hexagrams (based on data at $N = 30$); compared to estimated collapse time-scales. (c) Lightcone extracted for $\Delta = -1$ TFIM at $h/J = 0.75$ and $N = 30$ from equal-time two-point correlators $\langle \delta\sigma_z^r(t) \delta\sigma_z^{r=1}(t) \rangle$ to define t_L in subfigure (b). (d) $\Delta = 0$ TFIM at $h/J = 0.5$ at $N = 14$ exhibits distinct collapse and revival time-scales which we estimate based on spectrum properties [31].

serve that the scaling follows a power-law, Fig. 2c where the best power-law fit presents the dynamic transition point, $h/J = 1$ for integrable TFIM, which coincides with the phase boundary of equilibrium QPT. The extracted scaling exponent is $C_d \sim h^{1.54}$, far away from what we would obtain if we used ground state as the initial state and study DPT-I in TTC: $C_e \sim h^{2\beta}$ where $\beta = 0.125$ is the order parameter scaling exponent of Ising universality class. Hence, the extracted scaling exponent is genuinely dynamic and distinct from what could be predicted by using the theory of criticality [1, 30]. In conclusion, we report a new DPT scheme, where (i) one defines a hierarchy of timescales by a cutoff that is parametrized via the control parameter $t(h)$ based on excitation capacity of the model and (ii) studies a small interval of data at late timescale that leads to a well-defined non-equilibrium order.

Universality of the power-law scaling. Next, we break the integrability of TFIM via introducing the NNN spin coupling, $\Delta/J = -1$ in Eq. (1). As the model is interacting and nonintegrable, quasi-particle picture fails. Instead, we extract lightcones to define excitation (or correlation) speeds across the system via the fluctuations of equal-time correlators [32–35], $\langle \delta\sigma_z^r(t) \delta\sigma_z^{r=1}(t) \rangle$ where

$\delta\sigma_z^r(t) = \sigma_z^r(t) - \langle \sigma_z^r(t) \rangle$. While far away from the transition, lightcones are linear as in Fig. 3c [33, 34, 36], we find that closer to the phase boundary to disordered phase, linear cones turn into sublinear in both models [31]. In such cases, we approximate the sublinear cone with a linear one that works well for small distances to extract a lightcone velocity. Based on lightcone velocities we extract an h -parametrized cutoff whose form is given with dashed-black line in Fig. 3b fitted to purple-pentagrams and further matches well with grey-hexagrams that are blinded for testing the prediction power of the fit. We observe that a system size independent dynamic order emerges with a power-law in Fig. 2b after applying the DPT procedure in Fig. 1b, thus demonstrating the universality of power-law in our procedure. The power-law scaling exponent $C_d \sim h^{1.31}$ differs from the scaling exponent of the integrable TFIM, pointing out to the effect of interactions and nonintegrability in dynamic criticality. As we discuss in the next section, the observation that the scaling exponents depend on interaction strength $\beta_d(\Delta)$ is expected, because the emergent order, though dominated by GS contribution, consists of higher energy excitations where possible excitation energies increase towards the phase boundary. The transition point marked by the best scaling-law is $h/J = 2.025$, which is shifted from the equilibrium point $h_e/J = 2.46$ [31] in favor of disorder. Shifts from equilibrium phase boundary in nonintegrable TFIM are previously predicted in Ref. [21] for DPT-I with equal-time correlators averaged over space and demonstrated in Ref. [37] with OTOCs of infinite-temperature initial states in the context of dynamic topological order. Such shifts in phase boundary again suggest genuine non-equilibrium order. We emphasize that h -parametrized cuts that are defined for both models in this Manuscript are by no means, unique. In integrable TFIM, choosing larger late timescales eventually reaches to the infinite-time limit $t \sim N$ where the new DPT reduces to DPT-I, simply because the collected data is now the saturation value of the dynamic response, which is known to be featureless, [12, 19, 31]. On the other hand, studying smaller timescales would still provide a power-law scaling, however inducing shifts in the dynamic transition boundary from equilibrium, favoring disorder [31]. Parametric cuts in nonintegrable TFIM are even more flexible, given the numerical procedure to extract lightcone velocities. More generous cuts could generate dynamic order with transition boundary closer to equilibrium one. As a result, we note that via h -parametrized temporal cutoffs we can study a family of dynamic order with a distinct set of (h_d, β_d) parameters for each power-law scaling.

Non-equilibrium origin of the DPT. Given $|\psi_0\rangle = \sum_i c_i |\phi_i\rangle$ where $|\phi_i\rangle$ are eigenstates of the Hamiltonian, a TTC $C(t) = \langle \psi_0 | \sigma_r^z(t) \sigma_r^{z=1}(t) | \psi_0 \rangle = \langle \psi_0 | \sigma_r^z(t) | \psi_0 \rangle$ could

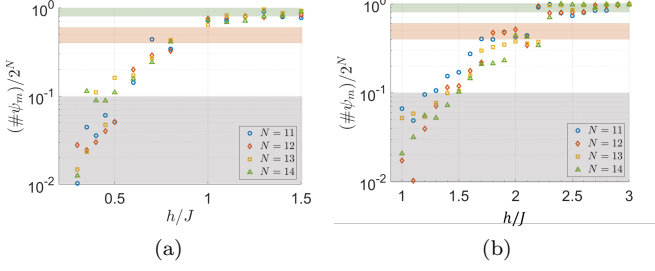


FIG. 4. The excitation ratio, $\#\psi_m/2^N$, plotted against the control parameter h/J for (a) $\Delta = 0$ and (b) $\Delta = -1$ TFIM. Grey, red and green boxes correspond to the lowest 0 – 10%, middle 40 – 60% and the highest energy sectors 80 – 100% of the whole spectrum.

be written as,

$$\sum_{ij} c_j^* c_i \langle \phi_j | \sigma_r^z | \phi_i \rangle e^{-it(E_i - E_j)} = \sum_{i \leq j} A_{ij} \cos[\delta_{ij}t]. \quad (3)$$

Eq. (3) can be used to estimate a hierarchy of timescales, e.g. quantum collapse and revivals based on the generalization of a method introduced in Ref. [38]. Here $A_{ij} = 2c_j^* c_i \langle \phi_j | \sigma_r^z | \phi_i \rangle$ is called overlap distribution and $\delta_{ij} = E_i - E_j$ is the energy gaps (see Supplement for details). Estimates for collapse and revivals for a system size of $N = 14$ are marked by τ_c (red-line) and $\tau_r^{(i)}$ (green lines), respectively, in Fig. 3d that demonstrates a dynamic response at $h/J = 0.5$ after quenched from a polarized state for integrable TFIM. We observe revivals in effectively infinite time limit $t \gtrsim N$, which is consistent with the fact that this is a region where finite-size effects appear. Estimated τ_c corresponds to a region where the dynamic response reaches its baseline before finite-size effects kick in. We estimate collapse time-scales for various h and plot them in Figs. 3a-3b for $\Delta = 0$ and $\Delta = -1$ TFIM, respectively. Remarkably collapse times exhibit the same trend with h -parametrized cutoff defined earlier based on maximum quasiparticle velocity; $\bar{\tau}_c \propto ah^{-1}$ where the coefficient a increases with system size, suggesting for large systems, $t_L(h)$ matches with collapse timescales. Same analysis for $\Delta = -1$ TFIM in Fig. 3b shows more clearly that our numerically determined h -parametrized cutoff is not unique and is a conservative bound.

Collapse timescales are contributed by many states. To demonstrate this, we determine the set of corresponding eigenstates of energy gaps that are found to be relevant in computing the collapse timescales; and mark the most energetic excitation as $\#\psi_m$. So, the system is capable of having excitations up to the corresponding energy E_m of eigenstate $\#\psi_m$, which results in a quantum collapse. Fig. 4 shows the excitation ratio $\#\psi_m/2^N$ for both models that reflects how much of the spectrum could be excited after the quench from a polarized state, when the

dynamical response is experiencing a quantum collapse. Data for different system sizes exhibit the same trend where $\#\psi_m/2^N$ steadily increases up until the phase boundary and saturates to $\#\psi_m/2^N \sim 1$ in the disordered phase, which is the maximum. This means that in the disordered phase the system is able to excite the highest energy levels, causing a fast collapse to zero baseline in TTC. We mark different thresholds on Fig. 4 with translucent boxes; grey, red and green correspond to the lowest 0 – 10%, middle 40 – 60% and the highest energy sectors 80 – 100% of the whole spectrum. Thus, the DPT order parameter seems to be contributed by states not only in the lowest sector of energy spectrum but also the higher energies as we approach QPT. This observation points to the true non-equilibrium nature of the DPT. Of course one can question then, how such a transient and dynamic quantity could still act as an order parameter that can mark a transition boundary which is reminiscent of the underlying equilibrium QPT. We emphasize that a dominant contribution of dynamic order is still from the ground state $C(t) = A_{max} + \sum_{i \leq j \neq gs} A_{ij} \cos[\delta_{ij}t]$ even for moderately large system sizes [31]. Although the GS contribution does decrease with system size [31] which is consistent with DPT-I being featureless, the contribution of higher energy states increases as seen in Fig. 4. This cooperation between GS and higher energy states results in a well-defined dynamic phase boundary for the DPT.

Conclusion. We introduced a new type of dynamical phase transition, which results in a system size independent, universal and dynamical power-law behavior, and is revealed by a control-parameter dependent temporal cut-off motivated by the excitation spectrum of the system, instead of a uniform and conventional $t \sim N$ cutoff. We showed that the dynamic phase boundary matches with equilibrium one in integrable TFIM, whereas it shifts by favoring disorder in nonintegrable TFIM. Extracted scaling exponents are distinct, pointing to the true non-equilibrium character of the dynamic order. We showed that the collapse times of the dynamic response coincide with the late timescales determined by h -parametrized cuts, further proving the non-equilibrium origin of the DPT. Our work opens new avenues to explore non-equilibrium order, with no need for reaching the saturation regime which is challenging for experiments [28]. There are interesting directions for future, as (i) how generic the new DPT procedure is for other short range Hamiltonians both in Ising and other universality classes, (ii) further whether it is applicable for long-range interacting models by devising h -parametrized cutoffs based on their logarithmic lightcones [39]; and (iii) if the new DPT could be observed in 2D Ising models.

Acknowledgments. We thank L.-M. Duan for his helpful suggestions. DMRG calculations are designed with ITensor [40] and performed by the Great Lakes High Performance Computing Cluster of the University of Michigan. This work was supported by National Science Found-

dition under Grant EFRI-1741618.

* cbdag@umich.edu

- [1] L. D. Landau, Zh. Eksp. Teor. Fiz. **7**, 19 (1937), [Phys. Z. Sowjetunion **11**, 26 (1937); Ukr. J. Phys. **53**, 25 (2008)].
- [2] J. Zinn-Justin, *Quantum Field Theory and Critical Phenomena; 4th ed.*, Internat. Ser. Mono. Phys. (Clarendon Press, Oxford, 2002).
- [3] S. Sachdev, *Quantum Phase Transitions* (Cambridge University Press, 2001).
- [4] W. H. Zurek, U. Dorner, and P. Zoller, Phys. Rev. Lett. **95**, 105701 (2005).
- [5] B. Damski and W. H. Zurek, Phys. Rev. Lett. **99**, 130402 (2007).
- [6] J. Dziarmaga, Advances in Physics **59**, 1063 (2010).
- [7] A. Polkovnikov, K. Sengupta, A. Silva, and M. Vengalattore, Rev. Mod. Phys. **83**, 863 (2011).
- [8] E. Nicklas, M. Karl, M. Höfer, A. Johnson, W. Muesel, H. Strobel, J. Tomkovič, T. Gasenzer, and M. K. Oberthaler, Phys. Rev. Lett. **115**, 245301 (2015).
- [9] M. Heyl, A. Polkovnikov, and S. Kehrein, Phys. Rev. Lett. **110**, 135704 (2013).
- [10] M. Heyl, Reports on Progress in Physics **81**, 054001 (2018).
- [11] T. Mori, T. N. Ikeda, E. Kaminishi, and M. Ueda, Journal of Physics B: Atomic, Molecular and Optical Physics **51**, 112001 (2018).
- [12] M. Heyl, F. Pollmann, and B. Dóra, Phys. Rev. Lett. **121**, 016801 (2018).
- [13] C. B. Dağ, K. Sun, and L.-M. Duan, Phys. Rev. Lett. **123**, 140602 (2019).
- [14] B.-B. Wei, G. Sun, and M.-J. Hwang, Phys. Rev. B **100**, 195107 (2019).
- [15] M. Eckstein, M. Kollar, and P. Werner, Phys. Rev. Lett. **103**, 056403 (2009).
- [16] B. Sciolla and G. Biroli, Phys. Rev. B **88**, 201110 (2013).
- [17] N. Tsuji, M. Eckstein, and P. Werner, Phys. Rev. Lett. **110**, 136404 (2013).
- [18] J. C. Halimeh, V. Zauner-Stauber, I. P. McCulloch, I. de Vega, U. Schollwöck, and M. Kastner, Phys. Rev. B **95**, 024302 (2017).
- [19] B. Žunkovič, M. Heyl, M. Knap, and A. Silva, Phys. Rev. Lett. **120**, 130601 (2018).
- [20] J. Zhang, G. Pagano, P. W. Hess, A. Kyprianidis, P. Becker, H. Kaplan, A. V. Gorshkov, Z. X. Gong, and C. Monroe, Nature (London) **551**, 601 (2017), arXiv:1708.01044 [quant-ph].
- [21] P. Titum, J. T. Iosue, J. R. Garrison, A. V. Gorshkov, and Z.-X. Gong, Phys. Rev. Lett. **123**, 115701 (2019).
- [22] F. H. L. Essler, S. Evangelisti, and M. Fagotti, Phys. Rev. Lett. **109**, 247206 (2012).
- [23] P. Calabrese, F. H. L. Essler, and M. Fagotti, Journal of Statistical Mechanics: Theory and Experiment **2012**, P07016 (2012).
- [24] P. Calabrese, F. H. L. Essler, and M. Fagotti, Phys. Rev. Lett. **106**, 227203 (2011).
- [25] M. Gessner, M. Ramm, T. Pruttivarasin, A. Buchleitner, H. P. Breuer, and H. Häffner, Nature Physics **10**, 105 (2014), arXiv:1311.4489 [quant-ph].
- [26] N. A. Sinitsyn and Y. V. Pershin, Reports on Progress in Physics **79**, 106501 (2016).
- [27] B. Neyenhuis, J. Zhang, P. W. Hess, J. Smith, A. C. Lee, P. Richerme, Z.-X. Gong, A. V. Gorshkov, and C. Monroe, Science Advances **3**, e1700672 (2017), arXiv:1608.00681 [quant-ph].
- [28] H.-X. Yang, T. Tian, Y.-B. Yang, L.-Y. Qiu, H.-Y. Liang, A.-J. Chu, C. B. Dağ, Y. Xu, Y. Liu, and L.-M. Duan, Phys. Rev. A **100**, 013622 (2019).
- [29] K. Xu, Z.-H. Sun, W. Liu, Y.-R. Zhang, H. Li, H. Dong, W. Ren, P. Zhang, F. Nori, D. Zheng, H. Fan, and H. Wang, arXiv e-prints, arXiv:1912.05150 (2019), arXiv:1912.05150 [quant-ph].
- [30] P. C. Hohenberg and B. I. Halperin, Rev. Mod. Phys. **49**, 435 (1977).
- [31] See supplementary material.
- [32] P. Calabrese and J. Cardy, Phys. Rev. Lett. **96**, 136801 (2006).
- [33] A. M. Läuchli and C. Kollath, Journal of Statistical Mechanics: Theory and Experiment **2008**, P05018 (2008).
- [34] M. Cheneau, P. Barmettler, D. Poletti, M. Endres, P. Schau, T. Fukuhara, C. Gross, I. Bloch, C. Kollath, and S. Kuhr, Nature **481**, 484487 (2012).
- [35] L. Villa, J. Despres, and L. Sanchez-Palencia, Phys. Rev. A **100**, 063632 (2019).
- [36] E. H. Lieb and D. W. Robinson, Communications in Mathematical Physics **28**, 251 (1972).
- [37] C. B. Dağ, L.-M. Duan, and K. Sun, Phys. Rev. B **101**, 104415 (2020).
- [38] C. B. Dağ, S.-T. Wang, and L.-M. Duan, Phys. Rev. A **97**, 023603 (2018).
- [39] M. Foss-Feig, Z.-X. Gong, C. W. Clark, and A. V. Gorshkov, Phys. Rev. Lett. **114**, 157201 (2015).
- [40] ITensor Library (version 2.0.11) <http://itensor.org>.

Supplementary: Dynamical scaling laws revealed by parametric temporal cutoffs

S1: DPT-I FOR TTC AND OTOC

Here we visualize the difference between OTOCs, $F(t) = \langle \psi_0 | \sigma_r^z(t) \sigma_{r'}^z(t) \sigma_r^z(t) \sigma_{r'}^z(t) | \psi_0 \rangle$ and TTCs $C(t) = \langle \psi_0 | \sigma_r^z(t) \sigma_{r'}^z(t) | \psi_0 \rangle$ in demonstrating persistent order, where $|\psi_0\rangle = |\uparrow\uparrow \dots \uparrow\rangle$ is a polarized state. Fig. S1a compares $F(t)$ and $C(t)$ for different system sizes N computed via time-dependent density matrix renormalization group (t-DMRG) at external field strength $h/J = 0.5$ in time spans of $t = N$. Hence in long time limit $t \rightarrow \infty$ which could effectively translate to $t \sim N$ for finite-size OTOCs, dynamical order persists indefinitely resulting in a well-defined dynamical phase boundary for the time-average or long-time saturation value \bar{F} in Fig. S1b, $h/J \sim 1$. Note that at $t \sim N$, $F(t)$ in Fig. S1a starts to demonstrate finite-size effects, illustrated with black circles, which justifies the argument that $t \sim N$ is the long-time limit $t \rightarrow \infty$ for chosen system sizes. In fact, such features in dynamics could be used to show the dynamical critical exponent $z = 1$ for Eq. (1) (Supp. Sec. S4). With the same reasoning, one can plot $C(t)$ in a time interval of $t = N$ in Fig. S1a and observe the decay of initial magnetization which dramatically becomes more pronounced as the system size increases, resulting in featureless long-time dynamics as well as a vanishing DPT boundary for \bar{C} in thermodynamic limit as seen in Fig. S1b.

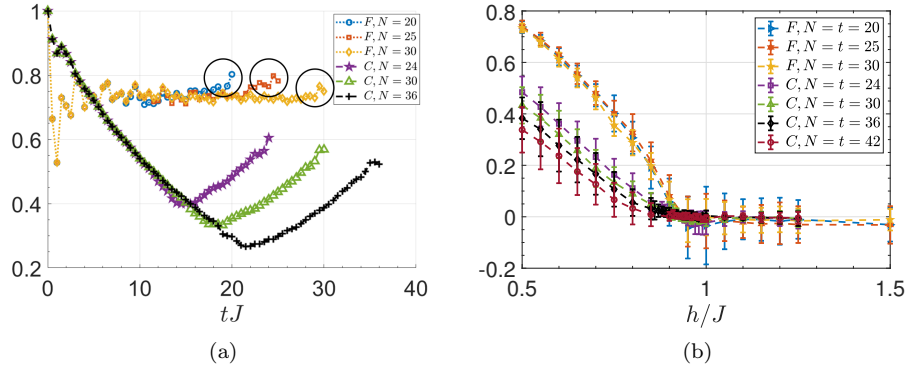


FIG. S1. (a) $C(t)$ and $F(t)$ for different system sizes N for integrable TFIM at $h/J = 0.5$; (b) DPT-I applied to $C(t)$ and $F(t)$ for a time interval of $t = N$ resulting in \bar{C} and \bar{F} with respect to control parameter h/J .

S2: LIGHTCONES BASED ON EQUAL-TIME TWO POINT CORRELATORS

In this section, we present more data on the lightcone structure of nonintegrable TFIM with $\Delta/J = -1$ quenched from a polarized state. One can obtain the lightcones and hence the correlation spread via the fluctuations of equal-time two-point correlators [S1–S4], $\langle \delta\sigma_z^r(t) \delta\sigma_z^{r=1}(t) \rangle$ where $\delta\sigma_z^r(t) = \sigma_z^r(t) - \langle \sigma_z^r(t) \rangle$ for all sets of $(r = 1, r > 1)$ running from $t = 0$ to some time t that reveals the functional form of the lightcone. Then we determine the contours of very small amplitude, ξ that sets the onset of fluctuations growing $\langle \delta\sigma_z^r(t) \delta\sigma_z^{r=1}(t) \rangle > 0$ for $t > 0$. Numerically one can study a set of lightcones with different ξ . We plot Fig. S2 for integrable TFIM for different $h = 0.5, 0.75, 0.9, 1$ which can already be analytically solved and hence the an h -parametrized cutoff could be defined based on the maximum quasiparticle velocity. We highlight contour thresholds ξ that visually reveal some lightcones and the extracted lightcone velocity is around the maximum quasiparticle velocity $v_L \sim v_{max}$. However we also note that according to field theory results, the lightcone effect should first appear at $v_L \sim 2v_{max}$ [S1]. This explains why we are able to see linear lightcones whose velocities are larger than the maximum quasiparticle group velocity v_{max} in Fig. S2. While we do find linear lightcones for h far away from the QPT [S2, S3, S5], e.g. $h = 0.5$ in Fig. S2a and $h = 0.75$ in Fig. S2b, interestingly closer to QPT the lightcones both visually and numerically turn into sublinear form, $x \propto t^\chi$ where $\chi < 1$. For small enough distances, we could approximate the sublinear cone with a linear one and determine a correlation velocity v_L , however for longer distances this approximation breaks down and the sublinear nature of the lightcones become even more pronounced.

In nonintegrable TFIM, we do not have a quasiparticle group velocity; hence the lightcone velocity v_L is the only well-defined quantity to determine the energetics of the excitations. As already discussed in the main text in detail, this

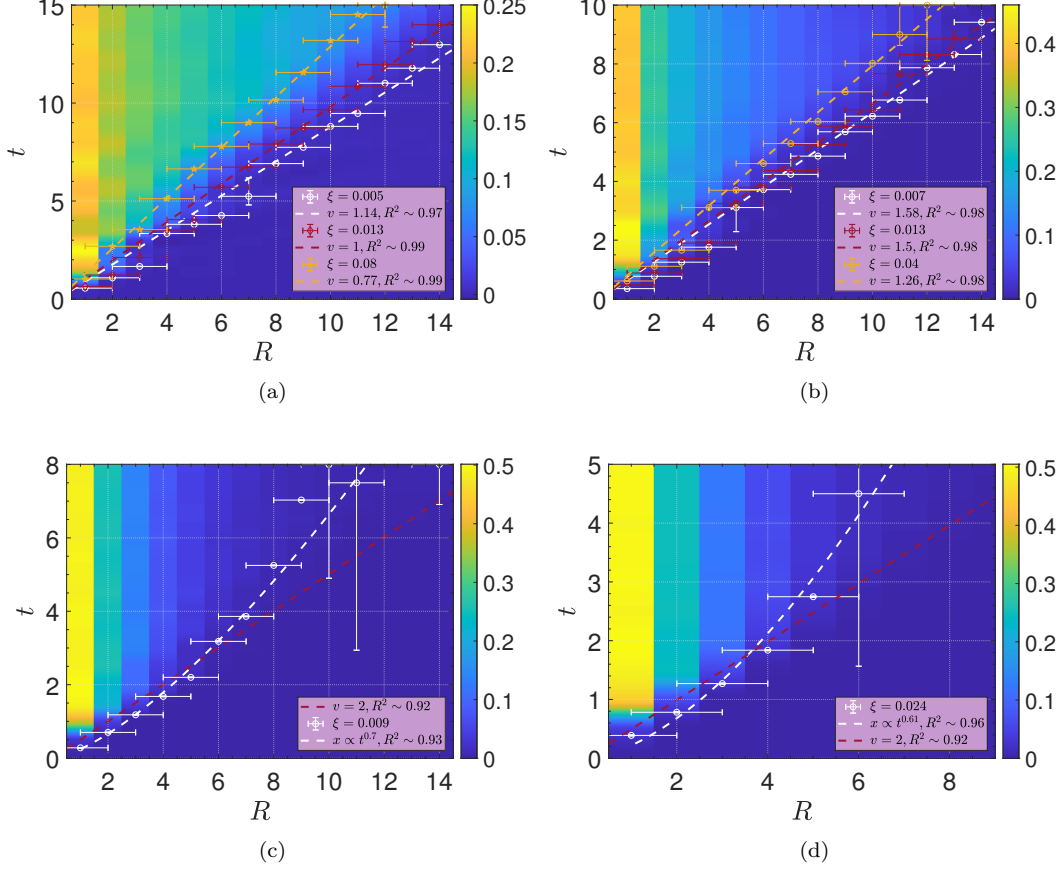


FIG. S2. Lightcones of integrable TFIM at (a) $h/J = 0.5$, (b) $h/J = 0.75$, (c) $h/J = 0.9$ and (d) $h/J = 1$ with system size of $N = 36$ via t-DMRG. In a lightcone figure, x- and y-axes stand for the spatial distance R and time t , respectively. The circles are the data points corresponding to the contour threshold ξ and the fitted dashed lines are the best fits to the data. R^2 in the legend is the correlation coefficient of the fit; v corresponds to the extracted lightcone velocity at its associated threshold value ξ . In subfigures (c) and (d), only one set of data is plotted with both sublinear (white dashed) and linear (red dashed) fitting models for convenient comparison.

makes the h -parametrized cutoff in nonintegrable TFIM a non-unique bound and opens up the possibility of defining different sets of dynamic phase boundaries with (h_d, β_d) . We plot lightcones of various $h = 0.5, 1, 1.2, 1.5, 1.75, 2$ in Fig. S3. Here as well, the linear lightcones far away from the QPT turn into sublinear forms as we approach the QPT. Different from the Fig. S2, we start comparing two fitting models deep in the ordered phase, $h/J = 1$ since the data of smaller h has both visually and numerically appealing linear lightcones, Fig. S3a and Fig. 3c (in the main text). Beginning from $h/J = 1$ we could start seeing a difference between two fitting models, while the forms of these models differ more dramatically as we come closer to QPT around $h/J \sim 2.025$, as we marked it in the main text. We determine the h -parametrized cutoff presented in the main text based on the linear fitting model that works well for small distances.

One can argue that the linearity of lightcones breaks down for large distances, given that the lightcones of only small distances are numerically and experimentally studied in the literature and found to be linear [S2, S3]. Whether emerging sublinear lightcones occur due to critical slowdown is an interesting future direction to follow.

After extracting lightcone velocities for different contour threshold values ξ at various h , we plot the calculated late time $t_L = 10/v_L$ with respect to ξ in Fig. S4a and based on this data we select three threshold values depicted by black vertical lines in the same figure. The data of these thresholds $\xi = 0.0005, 0.001, 0.002$ are plotted in Fig. S4b and fitted to extract a functional form for the h -parameterized cutoff. We use the most conservative bound that we found, namely the fit with blue dashed lines in our analysis of the DPT with nonintegrable TFIM.

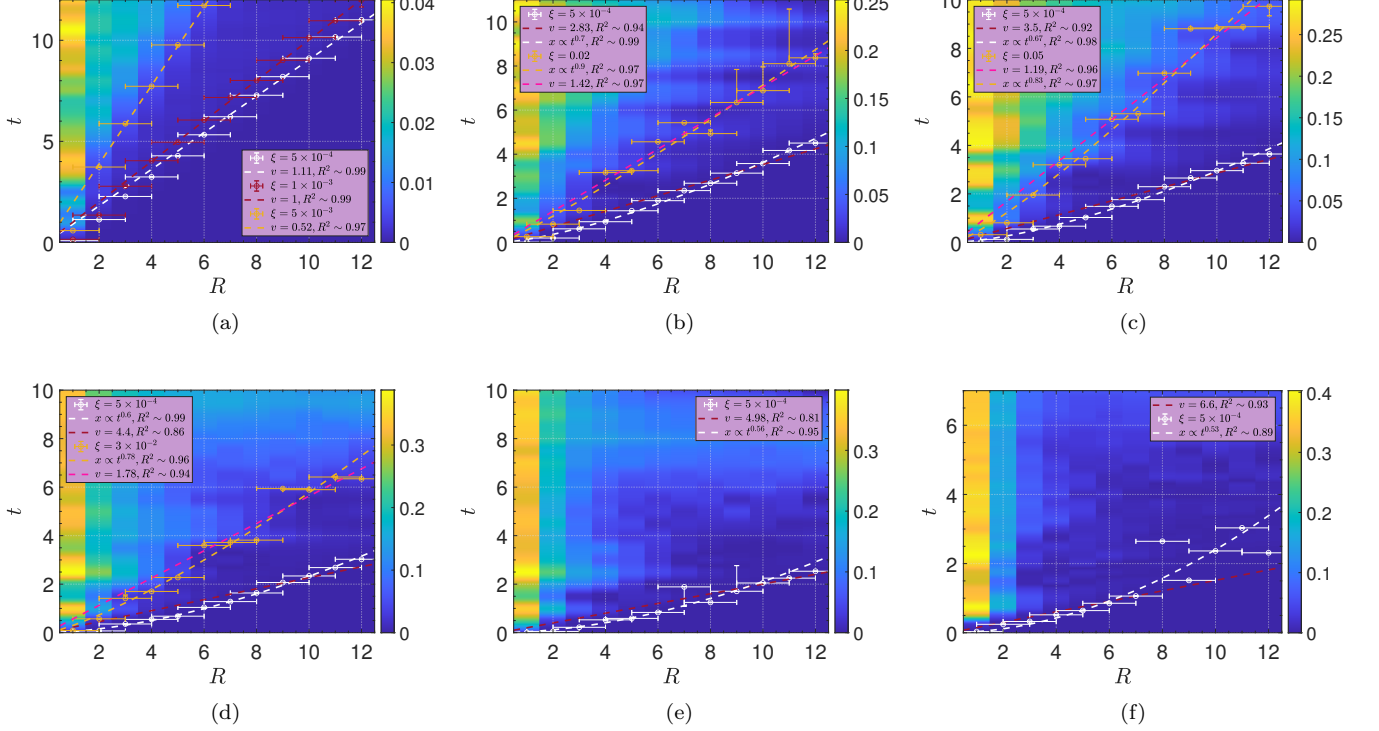


FIG. S3. Lightcones of nonintegrable TFIM with $\Delta/J = -1$ at (a) $h/J = 0.5$, (b) $h/J = 1$, (c) $h/J = 1.2$, (d) $h/J = 1.5$, (e) $h/J = 1.75$ and (f) $h/J = 2$ with system size of $N = 30$ via t-DMRG. In a lightcone figure, x- and y-axes stand for the spatial distance R and time t , respectively. The circles are the data points corresponding to the contour threshold ξ and the fitted dashed lines are the best fits to the data. R^2 in the legend is the correlation coefficient of the fit; v corresponds to the extracted lightcone velocity at its associated threshold value ξ . In subfigures (b) to (f), the sets of data are plotted with both sublinear (white dashed and orange dashed) and linear (red dashed and pink dashed) fitting models for convenient comparison.

S3: NON-EQUILIBRIUM ORIGIN OF THE DPT: DETAILS

Previously, Ref. [S6] put forward analytical estimations for the timescales of quantum collapse and revivals based on spectrum characteristics, such as energy gaps $\Delta_{ij} = E_i - E_j$ and (eigenstate occupation) overlap distributions $A_{ij} = 2c_j^* c_i \langle \phi_j | \sigma_r^z | \phi_i \rangle$, where c_i are eigenstate occupation numbers and ϕ_i are eigenstates in

$$C(t) = \sum_{i \leq j} A_{ij} \cos[\delta_{ij} t]. \quad (\text{S1})$$

Fig. S5a shows overlap distribution with respect to gaps for $\Delta = 0$ TFIM with system size of $N = 14$. The model under study in Ref. [S6] was a spinor condensate with single mode approximation applied, which simplified the estimations greatly, by focusing only on the first off-diagonal entries of the overlap distribution and the energy gaps [S6]. Here we observe that such a simplification is not possible, because there is not really a pattern of matrix elements that are occupied. Hence we need to generalize this method for irregular distributions like in Fig. S5a and predict a hierarchy of timescales, such as quantum collapse and revivals.

We first reshape the upper (or equivalently lower) triangular part of our overlap A_{ij} and energy gap δ_{ij} matrices into one dimensional arrays with keeping the relation between them intact. This results in Fig. S5a where y-axis stands for the norm of overlap distribution $|A_{ij}|$ and x-axis for the energy gaps δ_{ij} . Even though this does not give a regular distribution, e.g. a Gaussianlike distribution as in Ref. [S6], it still reveals the information necessary to utilize the timescale estimations of quantum collapse and revivals. The analytical estimation for quantum collapse reads,

$$t_c = 2\pi / (\delta_{max+\sigma} - \delta_{max-\sigma}), \quad (\text{S2})$$

where $max + \sigma$ is 1σ standard deviation around the point with maximum amplitude. The reasoning behind this estimation is that finding all relevant data that interferes destructively to give rise to a quantum collapse. We

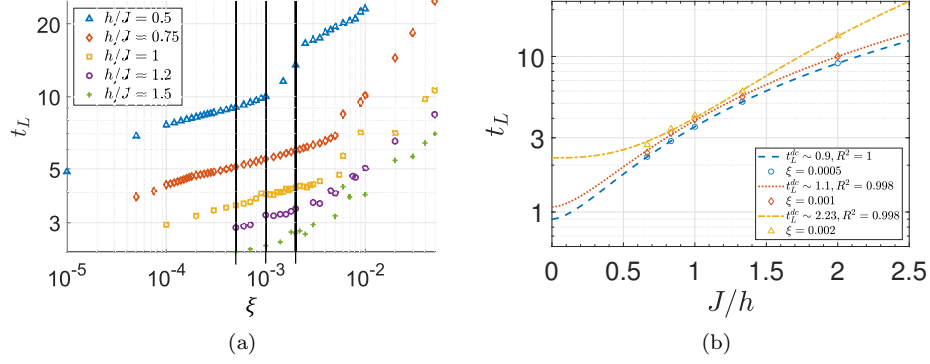


FIG. S4. (a) Late time t_L extracted for each contour threshold on lightcone ξ for different h values (see legend) and nonintegrable TFIM, $\Delta/J = -1$ at size $N = 30$. All data is calculated via t-DMRG. (b) Three different thresholds ξ are plotted against h/J and fitted with lines to numerically determine the functional form of the h -parametrized cutoff. These thresholds are shown with black vertical lines in subfigure (a).

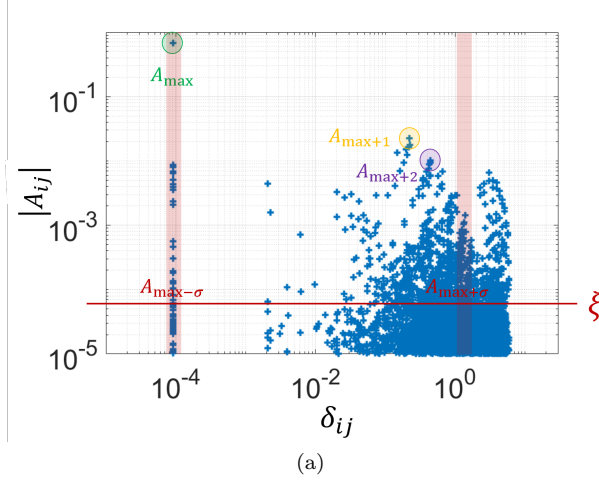


FIG. S5. The norm of overlap distribution $|A_{ij}|$ with respect to energy gaps δ_{ij} exhibiting features to estimate distinct timescales of dynamical response. The global and local maxima are circled with green, yellow and purple. The threshold ξ shows 1σ deviation from the maximum of all data, hence helping to determine the collapse timescale (see supplement text). Red translucent boxes show the area to utilize to determine the collapse timescale.

calculate the standard deviation of all data and this provides 1σ variation line, which is denoted by the threshold symbol ξ in Fig. S5a. Any data intersecting with threshold ξ is a valid data to obtain a collapse timescale. In a regular distribution with a single collapse timescale, there is only one data; however we see that in our overlap distribution we have a set of them. This is not surprising given various oscillatory features in real-time response, which is mostly the finite-size effects (Fig. 3d and others with larger system sizes). At this stage, detecting where the quantum revivals reside in overlap distribution is helpful to determine the correct collapse timescale. The analytical estimation for quantum revivals reads,

$$t_r^{(i)} = 2\pi/(\delta_{\max} - \delta_{\max+i}). \quad (\text{S3})$$

Originally $i = 1$ only, however we have different local maxima in our overlap distribution, Fig. S5a and hence we could have $i \geq 1$. Here δ_{\max} is the energy gap of the maximum of overlap distribution A_{ij} and as already mentioned $\delta_{\max+i}$ is the energy gap of the local maxima. We observe three clear local maxima in Fig. S5a which of two are circled with yellow and purple. The highest local minima and vicinity of it (circled with yellow) gives the timescale of the quantum revival marked with $\tau_r^{(1)}$ on Fig. 3d which is already deep in the effectively infinite-time limit and dominated by finite-size effects. The second local minima and its vicinity (circled with purple) gives the timescale of the first ever quantum revival that we mark as $\tau_r^{(2)}$ on Fig. 3d. Note that this revival also marks the onset of

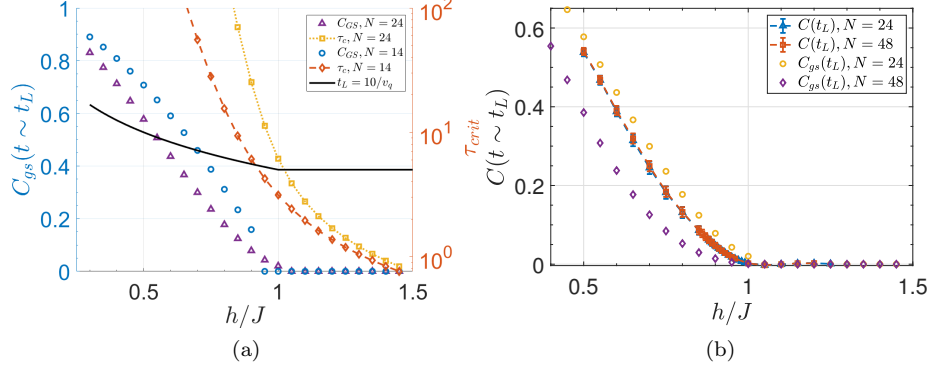


FIG. S6. (a) GS contribution (left y-axis) and critical time τ_{crit} (right y-axis) for $N = 14$ with exact diagonalization and $N = 24$ with DMRG. Black-solid line is late times t_L and should be compared with τ_{crit} . (b) GS contribution $C_{gs}(t \sim t_L)$ (DMRG) and the DPT order parameter $C(t \sim t_L)$ (t-DMRG) for $N = 24$ and $N = 48$. In both subfigures, x-axis is the control parameter h/J .

effectively infinite time. Marking these two most obvious quantum revivals in the dynamic response lets us limit our attention to times less than the timescale of the first revival. Times less correspond to energy gaps greater, due to the relation between two, Eq. (S2). Hence we look for the collapse timescale by focusing on the right hand side of the distribution in Fig. S5a. By obtaining a set of fewer and localized times for the quantum collapse, we mark the collapse timescale by averaging this set. The average of the estimated collapse time is marked with red vertical line and the 1σ deviation from the mean, with the translucent area around it in Fig. 3d.

Finally we elaborate on the contribution of ground state on the DPT order parameter. We first compare the GS contribution in TTC in a small-sized ($N = 14$, ED) and a larger size ($N = 24$, DMRG) systems in Fig. S6a with blue circles and purple triangles, respectively belonging to the left y-axis. The GS contribution in the DPT order parameter, analytically reads,

$$C_{gs}(t \sim t_L) = \sum_{i,j=gs} A_{ij} \cos(\delta_{ij}t). \quad (S4)$$

In the following discussion, let us call δ_{12} for δ_{ij} where $i, j = gs$. For a system in ordered phase and thermodynamic limit, $\delta_{12} = 0$ because of the symmetry-breaking ground state degeneracy, giving $C_{gs}(t \sim t_L) = \sum_{i,j=gs} A_{ij}$. However finite-size effects lift the degeneracy, $\delta_{12} > 0$, in particular as we approach closer to QPT. Hence we see the sudden drop to zero in $C_{gs}(t \sim t_L)$ of $N = 14$ system size with blue circles close to QPT, in contrast to smoother transition boundary as in $N = 24$ system size. We emphasize that this discontinuous feature in the dynamic response has nothing to do with the nature of the transition, rather it is a sign of how finite-size effects show up in data through our definition of a manual cutoff. Such effects also exist in previous research [S7]. To further strengthen this argument, we plot a quantity called critical time τ_{crit} which is governed by the degeneracy lifting as

$$\tau_{crit} = \frac{\pi}{4\delta_{12}}. \quad (S5)$$

We plot τ_{crit} for system sizes mentioned above in Fig. S6a with the right hand side y-axis. Note how τ_{crit} increases with increasing system size. We also plot t_L with black-solid curve in Fig. S6a which is determined by the maximum quasiparticle velocity and is used in the DPT. Comparing t_L with τ_{crit} helps us observing where the finite-size effects kick in, in the ordered phase. As soon as $\tau_{crit} < t_L$, finite-size effects start to be seen in $C_{gs}(t \sim t_L)$. Finally Fig. S6a also gives us an idea about the ground state contribution as system size increases. GS contribution $C_{gs}(t \sim t_L)$ clearly decreases as system size increases, which is a consistent observation with DPT-I being featureless for TTCs of locally connected Hamiltonians. To further demonstrate the non-equilibrium effects in our new DPT, we plot Fig. S6b for system sizes $N = 24$ and $N = 48$. GS contribution $C_{gs}(t \sim t_L)$ further decreases, whereas the DPT order parameter $C(t \sim t_L)$ is well-defined, as already presented in the main text. Hence this observation clearly tells us that, even though the dominant contribution in DPT order parameter is the GS contribution even in moderately large system sizes that we can access via t-DMRG, excitations to higher energy levels due to non-equilibrium procedure of the DPT do complement the dynamical order, thus providing a well-defined dynamic phase boundary. Perhaps this could be more straightforwardly seen in Fig. S5a, given that collapse time-scale is contributed by all states between $\delta_{max} + \sigma$

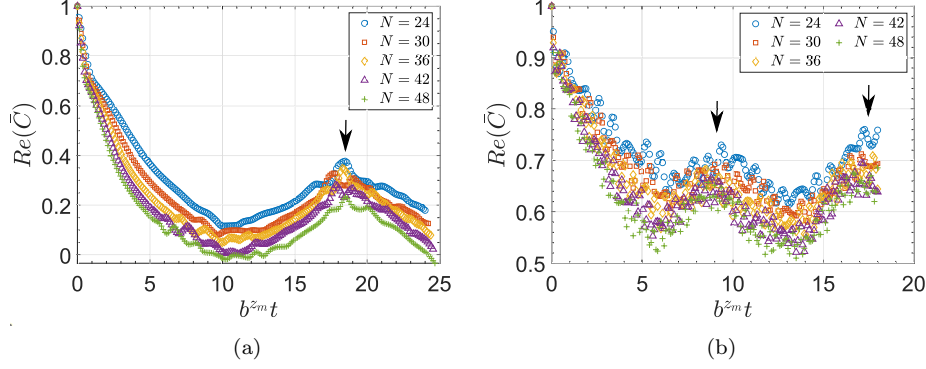


FIG. S7. $C(t)$ for different system sizes whose time axis is rescaled with b^{z_m} according to the scaling Ansatz written in the Supplement text for (a) integrable TFIM at $h/J = 0.7$ and (b) nonintegrable TFIM at $h/J = 1$. z_m is the optimized critical exponent extracted from the best alignment of data based on their finite-size effects which are denoted by black arrows.

and $\delta_{max-\sigma}$ with an overlap amplitude $A_{ij} > \xi$. Hence we observe that emergent dynamic order is indeed contributed by many states in the spectrum other than the ground state.

S4: DETERMINING THE DYNAMICAL CRITICAL EXPONENT z

Even though it is not clear if one can determine the critical exponents of correlation length ν , order parameter β and the anomalous dimension η (of TTCs) based on DPT-I, mainly because as shown in previous Supplement section the value of long time-average vanishes as we approach the thermodynamic limit which makes DPT-I not well-defined; we could still determine the dynamical critical exponent z via utilizing a scaling Ansatz. We show below the following scaling Ansatz could be observed via (auto) TTCs

$$C(r = r', t) = \chi(b) \mathcal{C}(b^z t), \quad (\text{S6})$$

where $\mathcal{C}(b, z, t)$ is the scaling function and χ is some unknown function of rescaling vector b . The reason why we write the unknown function $\chi(b)$ is because the amplitude of TTC $C(t)$ depends on system size, as it decreases as we approach the thermodynamic limit. However neither the functional form of this dependence is not clear, nor if there is a power-law behavior. This is again related to the fact that DPT-I is not well-defined for TTCs in locally connected Hamiltonians. However to determine the dynamical critical exponent, $\chi(b)$ does not need to be known. We could simply separate this component away and study the rescaling of time only. Fig. S7 shows TTC $C(t)$ figures of both (a) integrable ($h/J = 0.7$) and (b) nonintegrable TFIM ($h/J = 1$) for different system sizes calculated via t-DMRG and rescaled by b^{z_m} where z_m is to be found through optimization. We note that here the rescaling vector is fixed as $b = (N/N_{min})^{-1}$. We collect data for a time interval equal to the system size, e.g. for N , we measure $C(t)$ for $t = 0 : N$. The revivals of the dynamic response correspond to the finite size effects, denoted by black arrows in Fig. S7. We use these features of the dynamic response to align the data of different system sizes. Through this optimization procedure, we find that $z_m = 0.96$ in Fig. S7a and $z_m = 1$ in Fig. S7b. We note that we find the dynamical critical exponents for different h all close to $z_m \sim 1$ in ordered phase to phase boundary via the generalized scaling Ansatz of Eq. (S6) in both integrable and nonintegrable models.

S5: MARKING THE PHASE BOUNDARY OF EQUILIBRIUM QPT FOR COMPARISON

In this section, we present the equilibrium phase transition boundary via both an analysis of ground state energy gap and Binder ratio for the nonintegrable TFIM with $\Delta/J = -1$. Figs. S8a-S8b shows the determination of the phase boundary via energy gap analysis. We find that the equilibrium transition happens at $h_c \sim 2.463$ and the scaling exponent of the energy gap closing is $\delta \sim -1$. Further, we compute the Binder cumulant in Fig. S8c,

$$U = \frac{3}{2} \left(1 - \frac{1}{3} \frac{\langle S_z^4 \rangle}{\langle S_z^2 \rangle^2} \right), \quad (\text{S7})$$

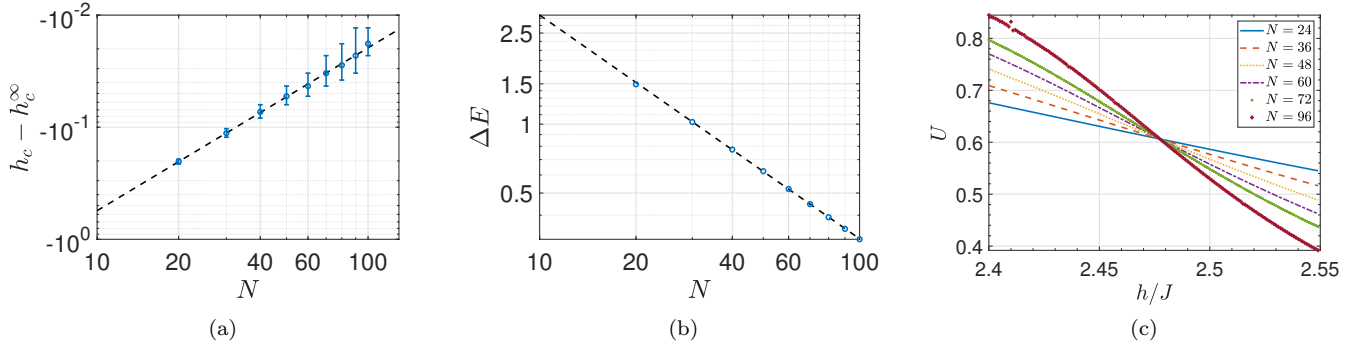


FIG. S8. (a-b) Ground state energy gap analysis with respect to system size N to determine the equilibrium quantum phase boundary. (a) The critical point is marked as $h_c^\infty = 2.463$ in thermodynamic limit via scaling analysis. (b) Energy gap ΔE closes as we approach the QPT boundary. The scaling exponent is $\Delta E = N^{-1}$. (c) Binder cumulant U for different system sizes ranging between $N = 24 - 96$, all crossing at $h_c = 2.477 \pm 0.001$.

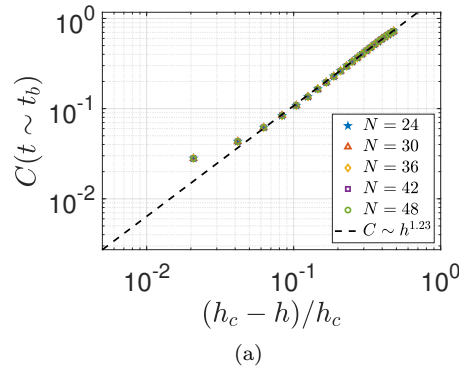


FIG. S9. The DPT power-law scaling of the dynamical order parameter in integrable TFIM with a h -independent cutoff at intermediate timescale. The transition boundary is marked as $h_{dc} \sim 0.96$ with a scaling exponent of $\beta_d \sim 1.23$.

where $S_z = \sum_i \sigma_i^z$, the total magnetization operator. This method marks the phase boundary as $h_c^\infty = 2.477 \pm 0.001$. The equilibrium transition boundaries determined by these two different methods are very close and hence we state that DPT boundary $h_{dc} \sim 2.025$ for the nonintegrable TFIM is very shifted from the equilibrium QPT.

S6: CHOOSING DIFFERENT TEMPORAL CUTOFFS

While choosing later times than Eq. (2) in the main text eventually reduces the new DPT to DPT-I, one can question what happens if we work with intermediate timescale, meaning well in the transient region. We observe a power-law scaling with the best fit marking the transition boundary as $h_{dc} \sim 0.96 < 1$ with a scaling exponent of $\beta_{dc} \sim 1.23$ in Fig. S9. Here we specifically choose a cutoff independent of h , however as mentioned, in an earlier timescale, $tJ = 5$. Note that, however, choosing even smaller times $tJ < 5$ likely not to be helpful anymore, since in such time interval the dynamic response would still be experiencing the collapse in the disordered phase, giving a nonzero contribution to dynamic order parameter of the DPT. We conclude that, via a cutoff in intermediate times, one can still obtain a power-law scaling however the transition point shifts in favoring disorder even in the integrable TFIM. Additionally the scaling exponent decreases compared to the h -parametrized cutoff chosen at late times.

* cbdag@umich.edu

[S1] P. Calabrese and J. Cardy, Phys. Rev. Lett. **96**, 136801 (2006).

[S2] A. M. Läuchli and C. Kollath, Journal of Statistical Mechanics: Theory and Experiment **2008**, P05018 (2008).

- [S3] M. Cheneau, P. Barmettler, D. Poletti, M. Endres, P. Schau, T. Fukuhara, C. Gross, I. Bloch, C. Kollath, and S. Kuhr, *Nature* **481**, 484487 (2012).
- [S4] L. Villa, J. Despres, and L. Sanchez-Palencia, *Phys. Rev. A* **100**, 063632 (2019).
- [S5] E. H. Lieb and D. W. Robinson, *Communications in Mathematical Physics* **28**, 251 (1972).
- [S6] C. B. Dağ, S.-T. Wang, and L.-M. Duan, *Phys. Rev. A* **97**, 023603 (2018).
- [S7] C. B. Dağ, K. Sun, and L.-M. Duan, *Phys. Rev. Lett.* **123**, 140602 (2019).